

1 **Spatially Varied Connections between Human Activity and**

2 **Satellite Observations in Tokyo**

3

4 **Abstract**

5 Human activity significantly affects urban economics, vitality, and development.

6 Owing to the availability of comprehensive and high-resolution satellite observations, a

7 variety of information of interest is obtained or estimated effectively and efficiently.

8 Satellite observations are generally proxied to represent and probe human activity.

9 However, substantial evidence to support the connections between human activity and

10 satellite data is relatively rare. Here, we use geographically weighted panel regression

11 (GWPR) to examine the relationship between low-speed transportation and several satellite

12 data, including nighttime light (NTL), greenness, temperature, as well as COVID-19-

13 related variables from January 2019 to December 2020. The accuracy of our model is

14 97.50%, and the model is reliable according to the 10-fold cross-validation. Our result

15 shows that a 1-unit increase in NTL in highly developed areas is associated with more

16 human activity growth. The only increased greenness in the publicly accessible parks could

17 attract more people, while warmer weather consistently increases low-speed transportation.

18 Overall, this research provides solid evidence to connect human activity and satellite data

19 to academia, governments, and societies.

21 **Keywords:**

22 Human Activity; Low-Speed Transportation; OD data; NTL; NDVI; Temperature;

23 GWPR

24

25 **Introduction**

26 With comprehensive and high-resolution satellite data, a variety of information,
27 including gross domestic product (Chen and Nordhaus, 2011; Li et al., 2013a), human
28 population distribution (Stevens et al., 2015), poverty (Jean et al., 2016; Yong et al., 2022),
29 urbanization (Sun et al., 2019), urban green space (Bellón et al., 2017), temperature (Li et
30 al., 2013b), air pollution (Li and Managi, 2022a), among others, could be obtained or
31 estimated effectively and efficiently. Among satellite data, nighttime light (NTL) products
32 are the most widely used in social science (Chen and Nordhaus, 2011). Previous studies
33 indicate that human activity is highly associated with NTL (Chen et al., 2019), and the
34 relationship is spatially non-stationary (Lan et al., 2021). However, several points can be
35 improved in the previous studies. First, the temporal resolution of the analyses in previous
36 studies is mainly annual, and some studies are even cross-sectional research. Moreover, the
37 density of point of interest (POI) is the index to represent human activity (Chen et al., 2019;
38 Lan et al., 2021; Wang et al., 2022). POI data generally contain several point types, such
39 as residential, business office, commercial service, among others (Wu et al., 2022). The
40 period of POI data updating is longer than satellite data, which makes the previous
41 researchers have to perform low temporal-resolution analysis. Furthermore, more POIs
42 attract more people to gather, consume, and do other activities. In a way, gathering people
43 is the main reason for economic development. Therefore, if the direct connection between
44 NTL and people are solidly built, the prediction and estimation of real human activity are
45 available with sufficient satellite data. Putting another way, human activity with the high
46 spatial and temporal resolution can be obtained with much lower cost.

47 To depict gathering people, we use low-speed transportation converted from the
48 origin-destination (OD) data based on the cell phone's location. With the availability of
49 OD data, more and more research uses them to investigate urgent issues (Shi et al., 2019;
50 Xiong et al., 2020). The urban activity pattern change has been detected by the OD data
51 (Shi et al., 2019). During the COVID-19 outbreaks, the relationship between human
52 mobility and COVID-19 infections is detected by the analyses of the OD data (Xiong et al.,
53 2020). Because the OD data from mobile devices are real-time and have accurate locations,
54 the dataset reflects human activity more frequently and effectively than POI data. In our
55 study, we take the monthly total low-speed transportation column as the proxy of human
56 activity. The movement speed of low-speed transportation is lower than 20 km/h, which is
57 mainly walking and cycling. Low-speed transportation is associated with urban economics.
58 Hence, the link between NTL and low-speed transportation is the primary evidence to
59 support the relationship between NTL and urban socioeconomic characteristics. However,
60 few studies focus on this topic because highly accurate OD data from mobile devices
61 gradually became available recently. Moreover, low-speed transportation is also affected
62 by several other variables, including greenness in the environment, temperature, among
63 others. Evidence shows that relatively greener environments could increase physical
64 activity (Caloguri and Elliott, 2017). Most people prefer to go outside in warmer weather.
65 Since our study period is from January 2019 to December 2020, the impacts of COVID-19
66 and the lockdown policy are also considered.

67 Furthermore, previous studies using POI data illustrate that the relationship
68 between NTL and human activity spatially varies. In this way, spatially local models are
69 required. Geographically weighted regression and multiscale geographically weighted

70 regression have been widely applied in previous studies (Lan et al., 2021; Wu et al., 2022).
71 However, these two models could only run pooled ordinary least square (OLS) on panel
72 datasets, which cannot eliminate the time-invariant individual effects. Our dataset is the
73 balanced panel spatial dataset. If necessary, the individual effects should be removed.
74 Recently, a novel method, geographically weighted panel regression (GWPR) is created,
75 which could take fixed-effect model (FEM) or random-effect model (REM) as the basic
76 regression model to solve the individual effects (Li and Managi, 2022a, b).

77 This study aims to probe the relationship between human activity and satellite data.
78 The study area is Tokyo, and the study period is from January 2019 to December 2020, for
79 a total of 24 months. The spatial and temporal resolutions are 250m and monthly,
80 respectively. A series of statistical tests show that GWPR is selected as the primary model.
81 Our GWPR model takes the low-speed transportation column as the dependent variable,
82 while NTL, greenness, temperature, COVID-19 prevalence, and lockdown ratio are the
83 independent variables in the analysis. Based on the variables of interest, we calibrate the
84 optimal fixed distance bandwidth of GWPR and estimate the spatially nonstationary
85 coefficients of the model.

86

87 **Materials and Methods**

88 ***Materials***

89 *Study Area*

90 Our study domain is Tokyo prefecture, with an area of more than 13,000 square
91 kilometers and more than 37 million residents, Japan's capital and largest city. **Figure 1**

92 demonstrates the study area, Tokyo. In fact, Tokyo has numerous outlying islands, but most
93 of them are small. Except Oshima Machi, no satellite data is available on the outlying
94 islands. Hence, in our study, we concentrate on the parts of Tokyo on Honshu island
95 (**Figure 1.B**) and Oshima Machi island (**Figure 1.C**). In order to improve data availability,
96 the Statistics Bureau of Japan divided the whole country into thousands of geospatial grids
97 with several spatial resolutions, including 80 km, 10 km, 1 km, 500 m, 250 m, and 125 m
98 (<https://www.stat.go.jp/english/data/mesh/05.html>). To combine with other data, we use a
99 250m spatial resolution dataset. In our study area, Tokyo has a total of 28,600 spatial grids.

100

101 *Origin-Destination Data (OD Data)*

102 The origin and destination locations are obtained from the cell phone's locations in
103 Tokyo. The location is not concrete longitude and latitude but the ID of regional mesh data.
104 Regional mesh data are the abovementioned geospatial grids. Service providers define that
105 if one person continuously stays in the same mesh grid for more than 15 minutes, the mesh
106 grid is deemed as an origin or a destination of a path. Additionally, the system reports all
107 detected movements every 15 minutes, including the paths' origin and destination mesh
108 grid IDs, estimated movement speed, and the total number of people on the paths. In the
109 hourly records, the locations of the first minute would be regarded as the origins, and the
110 locations of the last minute would be taken as the destinations. Since the other points are
111 ignored, we assume that all paths are considered straight lines, which is the shortcut
112 assumption. The estimated movement speed has three categories: slower than 20 km/h
113 (low-speed transportation), faster than 20 km/h but slower than 60 km/h (medium-speed
114 transportation), and faster than 60 km/h (high-speed transportation). In the raw dataset, the

115 medium-speed and high-speed transportation have few records. Furthermore, with
116 relatively high speeds, the assumption of lining up origins and destinations makes less
117 sense. Hence, the low-speed transportation column is investigated in this study.

118 The low-speed transportation column is the variable of interest because the low-
119 speed transportation column represents the amount of human activity and prosperity level.
120 Low-speed transportation mainly contains human walking and cycling. Based on the
121 shortcut assumption, all paths and numbers of movements on each path could be inferred
122 from the OD data. Then, the monthly low-speed transportation column of each mesh grid
123 could be extracted by the spatial join method. The temporal range of low-speed
124 transportation data is from January 2019 to December 2020, a total of 24 months. **Figure**
125 **2** demonstrates the temporally average value of the low-speed transportation column. In
126 the urban center, the low-speed transportation columns are extremely high, which are
127 generally over one million movements per month in each grid. In the suburbs, the low-
128 speed transportation columns mainly concentrate on the places close to the railway or
129 subway stations. The low-speed transportation columns are rare in the rural areas, the
130 western part (referring to **Figure 1**).

131

132 *Remote Sensing Data*

133 Several remote sensing data can indicate or be highly related to human activity,
134 including NTL (Huang et al., 2014; Wu et al., 2022), normalized difference vegetation
135 index (NDVI) (Brown et al., 2014; Pietrzyk-Kaszyńska et al., 2017), and temperature
136 (Krizek et al., 2009). The NTL data are widely applied to probe human activities and
137 economic status (Chen and Nordhaus, 2019; Chen et al., 2021; McCallum et al., 2022)

138 because busy transportation, road lighting, and commercial buildings bring artificial
139 electric light. The NTL data are extracted from other NASA products, Suomi National
140 Polar-orbiting Partnership Visible Infrared Imaging Radiometer Suite (NPPVIIRS)
141 nighttime light data. The earth observation group provides processed monthly NTL data
142 with a 1-km resolution. We use mesh grids with 250m to extract the NTL data. Although
143 the neighboring grids may have the same values, we still assume the values are the real
144 values of each grid. The unit of NTL is nanowatt per square centimeter steradian
145 ($nW/cm^2 \cdot sr$).

146 Temperature is associated with human activities (Krizek et al., 2009; Willis et al.,
147 2004). The temperature remote sensing data are available from NASA Moderate-resolution
148 Imaging Spectroradiometer (MODIS) products, MOD11A1 and MYD11A1, at a 1-km
149 spatial resolution. MOD11A1 product is generated by the NASA Terra satellite, while
150 MYD11A1 product comes from the NASA Aqua satellite. The temperature products
151 include daily daytime temperature and nighttime temperature. We average all temperature
152 rasters monthly and use the mesh grids to extract the monthly average temperature.

153 To examine the impact of greenness on low-speed transportation, we use the 16-
154 day level 3 NDVI data with 250-m spatial resolution. The NDVI data from NASA's
155 products, MOD13Q1 (<https://lpdaac.usgs.gov/products/mod13q1v006/>) and MYD13Q1
156 (<https://lpdaac.usgs.gov/products/myd13q1v006/>), are also from MODIS Terra and Aqua
157 Satellites, respectively. The NDVI is a graphical index to describe whether the observed
158 pixel contains live green vegetation and ranges from -1 (no live green vegetation, -100%)
159 to 1 (rife with live green vegetation, 100%) (Didan et al., 2015). We average the 16-day

160 data from Terra and Aqua into one raster. Monthly average NDVI values of each mesh grid
161 are extracted, which are considered the greenness level.

162

163 *COVID-19-related Variables*

164 The period of interest is from January 2019 to December 2020. In 2020, due to the
165 COVID-19 pandemic, Japanese local governments locked down the cities several times.
166 Apparently, during the lockdowns, low-speed transportation slashed dramatically.
167 Moreover, people's fear of the disease reduced human activities even without lockdowns
168 in 2020. To represent the impacts of lockdowns and fear of the disease on low-speed
169 transportation, we employ two variables, monthly lockdown ratio and monthly prevalence.
170 The monthly lockdown ratio is the ratio of days locked down in one month. For example,
171 if Tokyo locks down for 15 days in June, the monthly lockdown ratio is 0.5. The monthly
172 prevalence is in a specific month how many people get infected per 1,000 capita. When the
173 monthly prevalence is high, people are more afraid of the infection, which might eventually
174 reduce movements.

175

176 *Descriptive Statistics*

177 **Figure 3** illustrates the statistical distributions and descriptive statistics of the
178 variables in the original dataset. The statistical distribution of the low-speed transportation
179 column is one peak and right-skewed because the skewness is 4.02. Due to the 3.28
180 skewness, the statistical distribution of NTL is right-skewed. According to **Figure 3.b**,
181 there are two peaks in the distribution. The statistical distribution of NDVI is also two-

182 peak and almost symmetry since its skewness is 0.33, close to zero. The temperature's
183 statistical distribution is a slightly left-skewed one peak (skewness: -0.60). Since we
184 assume that every grid during a specific month has the same values of COVID-19-related
185 variables, the distributions of the monthly lockdown ratio and monthly prevalence are
186 relatively abnormal. Due to the distributions, using OLS directly without data
187 transformation is unsuitable.

188 To make the variables' statistical distributions more symmetry, we transform the
189 data to eliminate the time-invariant individual effects. The detailed processes of
190 elimination are reported in the next section. **Figure 4** demonstrates the variables'
191 distributions in the transformed dataset. After data transformation, although the
192 distributions of the low-speed transportation column, NTL and NDVI are seemingly more
193 symmetry, their skewnesses do not change much. Additionally, the kurtosises of these three
194 distributions increase significantly. The data transformation of temperature even makes the
195 situation worse. Its distribution becomes more skewed. According to the statistical tests,
196 data transformation is required but cannot solve the distribution issue. In fact, the
197 environments are significantly spatially diverse in Tokyo. The Western part is the city
198 center, and most people live there, while the Eastern region is mainly cropland and the
199 residential areas are sparse. Therefore, the global distributions are normally skewed and
200 leptokurtic. However, the distributions are more likely distributed in the geographically
201 local datasets. In this way, the geographically local regression is a better choice to analyze
202 the relationships among variables.

203

204 ***Methods***205 *Spatially Stationary Panel Model*

206 In the first stage, we assume that the relationships between low-speed transportation
 207 and other independent variables are spatially stationary (Brunsdon et al., 1998;
 208 Fotheringham et al., 2002). Pooled OLS model (POLS), FEM, and REM are widely used
 209 in spatially stationary panel data analysis. The difference among these three models is the
 210 time-fixed effects within individuals. To select rational time-fixed effects, we execute
 211 several necessary statistical tests. To compare FEM with POLS, we employ the F test for
 212 individual effects. The null hypothesis of the F test is that no time-fixed effects are needed
 213 (Breusch and Pagan, 1980; Croissant and Millo, 2008). The result of the F test is significant,
 214 indicating that FEM is better than POLS because the time-fixed effects exist. To compare
 215 REM and POLS, the Breusch-Pagan Lagrange Multiplier test for random effects is
 216 employed, whose null hypothesis is that no time-fixed effects are needed (Breusch and
 217 Pagan, 1980). The test result of our study is significant, representing that REM is better
 218 than POLS. The Hausman test is applied to compare FEM and REM (Kang, 1985). The
 219 significant result indicates that FEM is preferred since the null hypothesis that the preferred
 220 model is REM is rejected. Here, the FEM is as follows:

$$LST_{it} = \beta \mathbf{X}_{it} + \alpha_i + \mu_{it} \quad (1)$$

221 where LST_{it} represents monthly low-speed transportation in the mesh grid i during month
 222 t , \mathbf{X}_{it} represents a matrix of independent variables, including NTL ($nW/cm^2 \cdot sr$),
 223 temperature ($^{\circ}C$), NDVI, monthly lockdown ratio, and monthly prevalence
 224 (infections/1,000 capita) in the mesh grid i during month t , α_i represents the time-fixed

225 effects, μ_{it} represents an idiosyncratic error, and β is a vector of parameters to be
226 estimated.

227

228 *Spatially Non-stationary Panel Model*

229 REM, FEM, and POLS are spatially stationary models. In others words, the effects
230 of independent variables on low-speed transportation should always be the same no matter
231 where the location is. However, Tokyo's resources, including natural environments and
232 population, are not evenly distributed. Most people live in the urban zone of the eastern
233 part of Tokyo, while most natural environments locate in the western part of Tokyo.
234 Therefore, the effects of independent variable change might be spatially various.
235 Furthermore, the residuals of the stationary models might be spatially clustered. In this
236 study, we perform the panel Moran's I test to probe whether the residuals are spatially
237 clustered (Brunsdon et al., 2010; Fotheringham and Oshan, 2016). The I statistic of the
238 panel Moran's I test on FEM is 3.70 (p value < 0.1%), indicating that the residuals of the
239 FEM are spatially clustered. In this case, the spatially non-stationary panel model is more
240 suitable.

241 The GWPR has gradually become more prevalent in spatially non-stationary panel
242 analyses (Li and Managi, 2021, 2022a, b). The basic idea of the GWPR is that the attribute
243 of a certain location is similar to its neighbors. Hence, the GWPR divides the total dataset
244 into numerous local subsamples according to the optimal bandwidth. The GWPR
245 bandwidth is the furthest distance of two locations that can be regarded as the neighbors
246 (Beenstock and Felsenstein, 2019; Li and Managi, 2022a, b). Two types of bandwidth are
247 defined and applied, fixed distance bandwidth (Li and Managi, 2022b) and adaptive

248 distance bandwidth (Li and Managi, 2022a). If we use the fixed distance bandwidth, two
249 locations are neighbors of each other when their distance is smaller than the bandwidth.
250 The sample sizes might vary in each subsample divided by the fixed distance bandwidth.
251 In contrast, if we use the adaptive distance bandwidth, the sample sizes of each subsample
252 are the same. The threshold distance could change for each subsample to guarantee a stable
253 sample size. Since our analysis zone is a continuous area, the fixed distance bandwidth is
254 more rational and employed, as in previous studies (Li and Managi, 2022b).

255 The mean square prediction error of the model is used to calibrate the optimal
256 bandwidth. A lower mean square prediction error means that the model with this bandwidth
257 has the highest accuracy (Gollini et al., 2015). The mean square prediction error of the
258 GWPR model is calculated as follows:

$$MSPE(b) = \frac{m \sum_j [y_j - \widehat{y}_j(b)]^2}{(m - p + 1)^2} \quad (2)$$

259 where $MSPE(b)$ represents the mean square prediction error based on a specific bandwidth
260 b , m is the data size, y_j represents the low-speed transportation of the j th record, $\widehat{y}_j(b)$
261 represents the predicted low-speed transportation of the j th record by the GWPR model
262 with bandwidth b , and p is the number of parameters in the analysis. The unit of the
263 bandwidth b in this study is arc degree. The step increment selection has been widely
264 applied to calibrate the optimal bandwidth in previous studies (Li and Managi, 2022a, b).
265 The selection extent of interest is from 0.0025 arc degrees to 0.2 arc degrees, and the
266 examined bandwidth increases by 0.0025 arc degrees every time because the spatial
267 resolution of the mesh grid is 250m, approximately 0.0025 arc degrees. The optimal fixed
268 distance bandwidth is 0.015 arc degrees (**Figure 5**).

269 After the bandwidth is calibrated, the spatial weight vectors of each subsample are
 270 built. The spatial weight vector is calculated as follows:

$$\mathbf{W}_i = \begin{cases} [1 - (\frac{d}{b})^2]^2, & d_k \in \mathbf{d} \text{ if } d_k \leq b \\ 0, & d_k \notin \mathbf{d} \text{ if } d_k > b \end{cases} \quad (3)$$

271 where \mathbf{W}_i is the spatial weight vector of the subsample taking location i as the center, \mathbf{d}
 272 represents a vector of distances between center location i and other locations, b is the
 273 selected threshold distance, and d_k is the distance between location i and location k . Every
 274 vector is a column of the spatial weight matrix, which is $i \times i$. According to the spatial
 275 weight vectors, the total sample is divided into 28,600 subsamples, taking every mesh grid
 276 location as the center.

277 The GWPR estimates the coefficients in every mesh grid locally based on the
 278 spatial weight matrix. Since the FEM is the preferred spatially stationary model, the GWPR
 279 model also follows the FEM. The GWPR model is written as follows:

$$LST_{it} = \boldsymbol{\beta}_i \mathbf{X}_{it} + \alpha_i + \epsilon_{it} \quad (4)$$

280 where $\boldsymbol{\beta}_i$ represents a vector of parameters in the regression with the subsample taking
 281 mesh grid i as the center. It must be noted that $\boldsymbol{\beta}_i$ varies spatially.

282 In **Equation 4**, the time-fixed effects (α_i) are unknown (Croissant and Millo, 2008).
 283 To estimate the coefficient in the GWPR, the transformation of the equation is needed:

$$LST_{it} - \widehat{\theta}_i \overline{LST}_i = (1 - \widehat{\theta}_i) \beta_{0i} + \boldsymbol{\beta}_i (\mathbf{X}_{it} - \widehat{\theta}_i \overline{\mathbf{X}}_i) + (\epsilon_{it} - \widehat{\theta}_i \overline{\epsilon}_i) \quad (5)$$

284 where $\widehat{\theta}_i$ denotes the share of the time-fixed effects within individuals, \overline{LST}_i denotes the
 285 mean of the low-speed transportation in the mesh grid i , β_{0i} is the estimated intercept in
 286 the mesh grid i , $\overline{\mathbf{X}}_i$ denotes a vector of means of independent variables in the mesh grid i ,

287 and $\bar{\epsilon}_i$ denotes the mean of the error in the mesh grid i . In the FEM, $\hat{\theta}_i$ is always equal to
 288 1. Therefore, β_{0i} can be removed in each local regression. To simplify **Equation 5**, we
 289 define the matrix of independent variables \mathbf{x}_{it} , the dependent variable lst_{it} , and the
 290 residuals σ_{it} as follows:

$$\mathbf{x}_{it} = \mathbf{X}_{it} - \bar{\mathbf{X}}_i \quad (6)$$

$$gno2_{it} = GNO2_{it} - \bar{GNO2}_i \quad (7)$$

$$\sigma_{it} = \epsilon_{it} - \bar{\epsilon}_i \quad (8)$$

291 In light of **Equations 6-8**, the GWPR model can be rewritten as follows:

$$lst_{it} = \boldsymbol{\beta}_i \mathbf{x}_{it} + \sigma_{it} \quad (9)$$

292 Here, **Equation 9** is a weighted OLS. The coefficient can be estimated based on the
 293 transformed data and spatial weight matrix:

$$\boldsymbol{\beta}_i = [\mathbf{x}_{it}^T \mathbf{W}_i \mathbf{x}_{it}]^{-1} \mathbf{x}_{it}^T \mathbf{W}_i lst_{it} \quad (10)$$

294

295

296 Results

297 The overall accuracy of the GWPR according to FEM transformation is 97.50%.
 298 The root mean square error (RMSE) and mean absolute error (MAE) are 43374.91
 299 *Capita/(grid · month)* and 15854.20 *Capita/(grid · month)*, respectively, where the
 300 mean of low-speed transportation column per grid is 179335.80 *Capita/(grid · month)*.
 301 **Figure 6** displays the relationship between the predicted and measured low-speed
 302 transportation column in the GWPR model, and all coefficients in **Figure 6** are significant
 303 at a 0.1% level. The Pearson's correlation coefficient (r) between the predicted and

304 measured values is 0.987, a strong correlation. Furthermore, when we use OLS to fit the
305 relationship between measured and predicted values, the slope coefficient is 0.973 (p value
306 < 0.1%), and the intercept is 0.005 (p value < 0.1%). It must be noted that the unit of low-
307 speed transportation column is a million capita per grid per month. The ideal slope and
308 intercept are 1 and 0, respectively. To sum up, in total, our model accurately fits the
309 relationships among the variables.

310 To confirm the temporal stability of our model, we calculate all the monthly
311 statistical indicators. **Table 1** records the monthly statistical indicators, including R²,
312 RMSE, correlation coefficient (*r*), slope and intercept of regressions between measured
313 and predicted values. The lowest monthly R² is 78.14% in May 2020. The monthly RMSE
314 and MAE peak in June 2020, respectively, which are 89384.12 and 35769.02
315 *Capita/(grid · month)*. Additionally, the slope and intercept are the most different from
316 ideal values in the results of June 2020. The lowest *r* appears in the results of April 2020.
317 During this period, from April 2020 to June 2020, it was the first time that COVID-19
318 outbroke in Japan. The central government of Japan claimed a lockdown policy. Moreover,
319 since less is known about COVID-19, fear of the coronavirus further slashes people's
320 movement in Tokyo.

321 **Table 2** records the results of the 10-fold cross-validation of our model. In the 10-
322 fold cross-validation, the total dataset is randomly divided into ten subsets. In each single-
323 fold cross-validation, nine subsets are used to train the model, while the reserved subset is
324 employed to test the reliability of prediction. The lowest prediction accuracy for the test
325 subset is 79.52%, and its RMSE, MEA, and coefficient (*r*) of the correlation between the
326 predicted and measured values are 147820.50 *Capita/(grid · month)*, 38866.92

327 $\text{Capita}/(\text{grid} \cdot \text{month})$, and 0.888, respectively. The performance of our model is stable,
328 according to the results of the 10-fold cross-validation.

329 **Figure 7** displays the NTL coefficients in the GWPR model. The sense of the NTL
330 coefficient is that a $1-nW/cm^2 \cdot sr$ increase in NTL in a certain grid is associated with the
331 coefficient-value capita per month increase in the low-speed transportation column. The
332 spatial non-stationary NTL coefficients range from -2178.741 to 7795.078, with a mean of
333 738.560, whose 95% confidence interval (CI) is [727.225, 749.893]. According to **Figure**
334 **7**, in the urban center, $1-nW/cm^2 \cdot sr$ NTL is related to more low-speed transportation,
335 while in the rural regions, NTL is even negatively associated with detected people's
336 movement. Bright metropolitan areas gather more people and provide space for busy
337 human activity, so the urban center with high NTL value has more low-speed transportation.
338 Reversely, a large amount of human activity improves the economic vitality of the urban
339 center. In rural regions, relatively few people live there, and in most places, bright
340 environments do not attract more people to come. In the low population density regions,
341 the bright NTL is generally for safety or other aims rather than for walkers or bicycle riders.
342 Therefore, the relationship between NTL and low-speed transportation is negative in the
343 Western part of Tokyo.

344 **Figure 8** illustrates the NDVI coefficient, whose maximum and minimum are
345 21218.450 and -288729.900, respectively. The mean of the NDVI coefficients is -3126.589
346 (95% CI: [-3271.249, -2981.93]). In terms of the mean value and the spatial distribution of
347 the NDVI coefficients, more greenness is seemingly negatively linked to low-speed
348 transportation. In other words, greenness might reduce the possibility of human walking
349 and cycling, which is counterintuitive. We find that the positive NDVI coefficients sparsely

350 cluster in the metropolitan regions. Referring to the map, the positive zones are primarily
351 public parks without strict restrictions. The green places with restrictions typically have
352 negative NDVI coefficients. The Imperial Palace of Japan is a case in point. Public parks
353 would induce more human movement within them when their greenness increases.

354 **Figure 9** shows the temperature coefficients, ranging from -2422.258 to 93559.680,
355 with a mean of 3507.134 (95% CI: [3446.254, 3568.014]). In most places, the temperature
356 is positively correlated with low-speed transportation. Putting another way, people prefer
357 to walk and cycle in the warmer month. **Figures 10** and **11** illustrate the COVID-19
358 prevalence's and lockdown's effects on low-speed transportation. The maximum of the
359 COVID-19 prevalence coefficients is 236175.100, while the minimum is -7944757.000.
360 Their mean is -269288.100 (95% CI: [-277785.9, -260790.3]). Additionally, the lockdown
361 coefficients range from -1860805.000 to 1804.603, with a mean of -100161.900, whose
362 95% CI is [-102218.600, -98105.220]. In general, the outbreak of COVID-19 dramatically
363 slashes human movement. High prevalence makes the urban center silent. More people
364 might go to rural areas to avoid getting infected during outdoor activity, which leads to
365 positive COVID-19 prevalence coefficients in rural areas. However, the lockdown policy
366 almost cut down human movement anywhere.

367

368 **Discussion**

369 We use the GWPR model to probe the association of low-speed transportation from
370 OD data with satellite-derived data from January 2019 to December 2022 in Tokyo. In the
371 250m grid-level analysis, the model grasps relatively accurate spatial non-stationary

372 relationships among variables because the model's accuracy is 97.50%. As far as we know,
373 this is the first study that uses the spatial panel model with a high temporal and spatial
374 resolution to probe the connection between NTL and human activity. In the 10-fold cross-
375 validation, the accuracy of testing dataset prediction in every single iteration is around 80%,
376 indicating high robustness. Based on this highly accurate model, the long-believed
377 connection between NTL and human activity is substantially proved. Brighter places have
378 more human activity, although this relationship is not evenly globally consistent.

379 Previous studies indicate that the connection between NTL and human activities is
380 solid (Chen et al., 2019; Huang et al., 2014; Wu et al., 2022). However, the previous
381 research mainly uses the kernel density of point of interest (POI) to represent human
382 activity (Huang et al., 2014; Wu et al., 2022). POI datasets can indicate several types of
383 human activity, but their temporal resolution is relatively low. Most of them are even cross-
384 sectional, e.g., (Chen et al., 2019; Wu et al., 2022). Cross-sectional analyses should
385 consider more conditions because individual time-invariant effects cannot be eliminated.
386 To solve this issue, previous studies employ spatially non-stationary models from the
387 geographically weighted regression family, such as geographically weighted regression
388 and multiscale geographically weighted regression (Liu et al., 2020; Wu et al., 2022), and
389 machine learning methods, like random forest (Wang et al., 2020). In our study, we exploit
390 low-speed transportation converted from OD data to denote human activity. Our low-speed
391 transportation's spatial and temporal resolution is high compared to POI datasets used in
392 previous research. With high-resolution low-speed transportation and satellite datasets, the
393 individual time-invariant effects can be eliminated in our study, which helps us further
394 increase the model accuracy. Our studies also illustrate the relationship between human

395 activity and NTL spatially varies, consistent with previous studies (Liu et al., 2020; Wu et
396 al., 2022). Since the dependent variable is how many people pass a certain grid in a specific
397 month, this study links NTL and low-speed transportation more concretely.

398 The relationship between greenness and human activity is spatially non-stationary
399 (Zhong et al., 2020). Urban greenness generally positively impacts human activity (Brown
400 et al., 2014; Pietrzyk-Kaszyńska et al., 2017). On the one hand, the relationship between
401 greenness and human activity is counterintuitive because, in most places in Tokyo, the
402 effects of an increase in greenness are negative. There are several reasons for the adverse
403 effects. First, the greenness index is monthly NDVI, while in the previous studies, the
404 greenness data are mainly land cover or land use data. The land cover or land use data are
405 normally annual. Additionally, the land cover or land use variation is not apparent in the
406 short term. Second, Tokyo is a developed city. It is not easy to build ample green space in
407 Tokyo suddenly. Therefore, the greenness change is induced by the season shift. The
408 season shift influences other variables, including NTL (Chen et al., 2019) and temperature.
409 Third, Tokyo's development intensity is too high in the urban center. According to the
410 30m-resolution land cover dataset from the Japan Aerospace Exploration Agency, some
411 grids even have only impervious land cover. In these grids, even though there is sparse
412 greenness, their alteration would not draw people's attention, let alone attract more people
413 to come. On the other hand, in public accessible parks with a variety of greenness, the
414 increase in greenness significantly leads to more movement. In fact, previous studies
415 mainly mention and concentrate on urban green space (Zhong et al., 2020). Parks are a
416 major part of urban green space. Hence, our study is still in line with previous studies.

417 Human movement is related to the environment's temperature, as proved by
418 previous research (Krizek et al., 2009; Willis et al., 2004). In our study, the monthly
419 average temperature is almost always positively associated with low-speed transportation.
420 The reason is mainly due to the geographical location of Tokyo. Since Tokyo is in the
421 North temperate zone and close to the Pacific, the high temperature in summer is not
422 extreme. The increased temperature there makes people more willing to walk or cycle.
423 Moreover, COVID-19-related variables, including prevalence and lockdown ratio,
424 primarily negatively affect human movement. Previous studies also observed the negative
425 impact of COVID-19 on human activity using NTL data (Lan et al., 2021; Liu et al., 2020;
426 Wang et al., 2022). Our results tally with those studies in terms of the impacts of COVID-
427 19.

428 Some limitations remain in our study. First, some hidden variables are ignored. For
429 example, meteorological variables, such as wind speed, humidity, precipitation, among
430 others, are not included in the analysis. Second, since we cannot observe the real routes of
431 each movement, we replace straight lines from origins to destinations with real routes. The
432 record period is 15 minutes. If the movement speed reaches the limit of low-speed
433 transportation, 20km/h, the movement should be 5km. Using straight lines is not so
434 suitable in a way. Third, the COVID-19-related variables are spatial stationary, and the
435 spatial resolution of NTL and temperature is relatively lower than the low-speed
436 transportation column. Future studies should focus on the following topics. First, more
437 variables, such as high temporal-resolution land cover and POI, among others, need to be
438 included in future analyses. Second, combined with maps and machine learning, the
439 method to generate paths should be improved.

440

441 **Conclusions**

442 This study employs a high-accuracy GWPR model to detect the spatially non-
443 stationary relationships between monthly human activity and several satellite data at a
444 250m spatial resolution. The GWPR model exhibits excellent accuracy (97.50%), r value
445 (0.987), RMSE (43374.91 $\text{Capita}/(\text{grid} \cdot \text{month})$) and MAE (15854.20
446 $\text{Capita}/(\text{grid} \cdot \text{month})$) in the fitting process and stability in the cross-validation. In the
447 urban center, a $1-nW/cm^2 \cdot sr$ increase in NTL is associated with more human activity
448 growth. The only increased greenness in the publicly accessible parks could attract more
449 people. In warmer weather, people prefer to have more movement. Our results provide
450 solid evidence to connect human activity and satellite data, which helps governments and
451 societies to formulate more reasonable and efficient public policies.

452

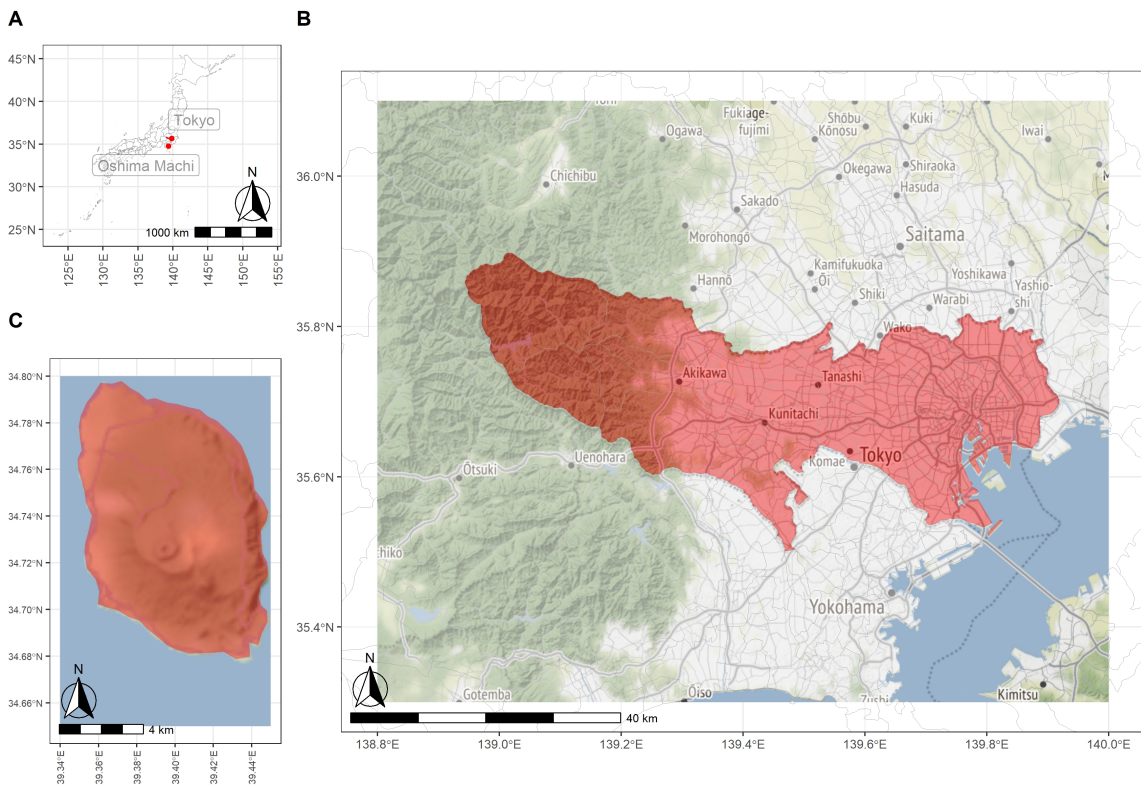
453 **Data Availability**

454 All data sources used in the analyses, along with fully reproducible code, are
455 publicly available at [https://github.com/MichaelChaoLi-](https://github.com/MichaelChaoLi-cpu/Low_Speed_Transportation_Satellite)
456 [cpu/Low_Speed_Transportation_Satellite](https://github.com/MichaelChaoLi-cpu/Low_Speed_Transportation_Satellite).

457

458

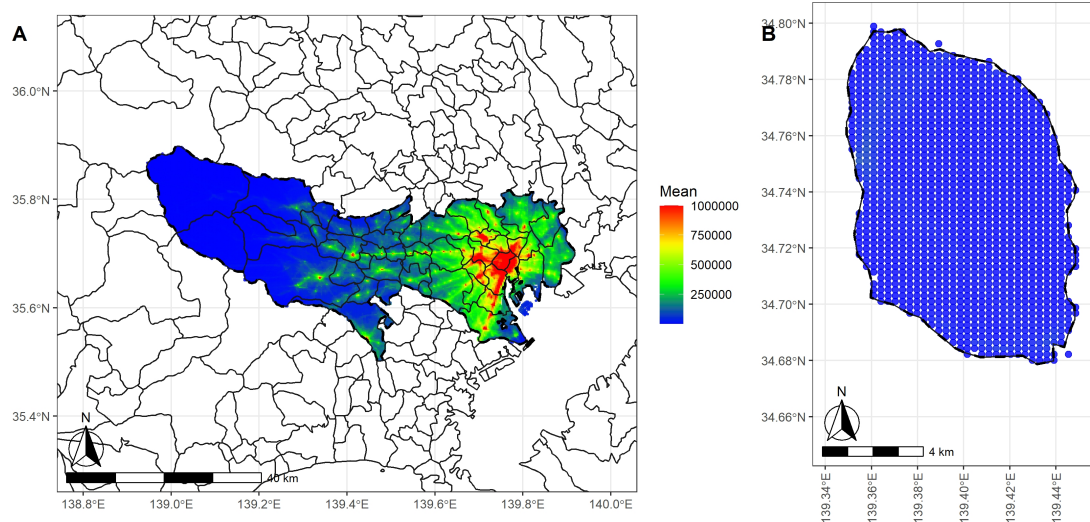
459 **Figure**



460

461 **Figure 1: Study Area and Its Location**

462 (a: Tokyo's location in Japan; b: the part of Tokyo on Honshu Island; c: the Oshima
463 Machi part of Tokyo, hereinafter called Oshima Machi)

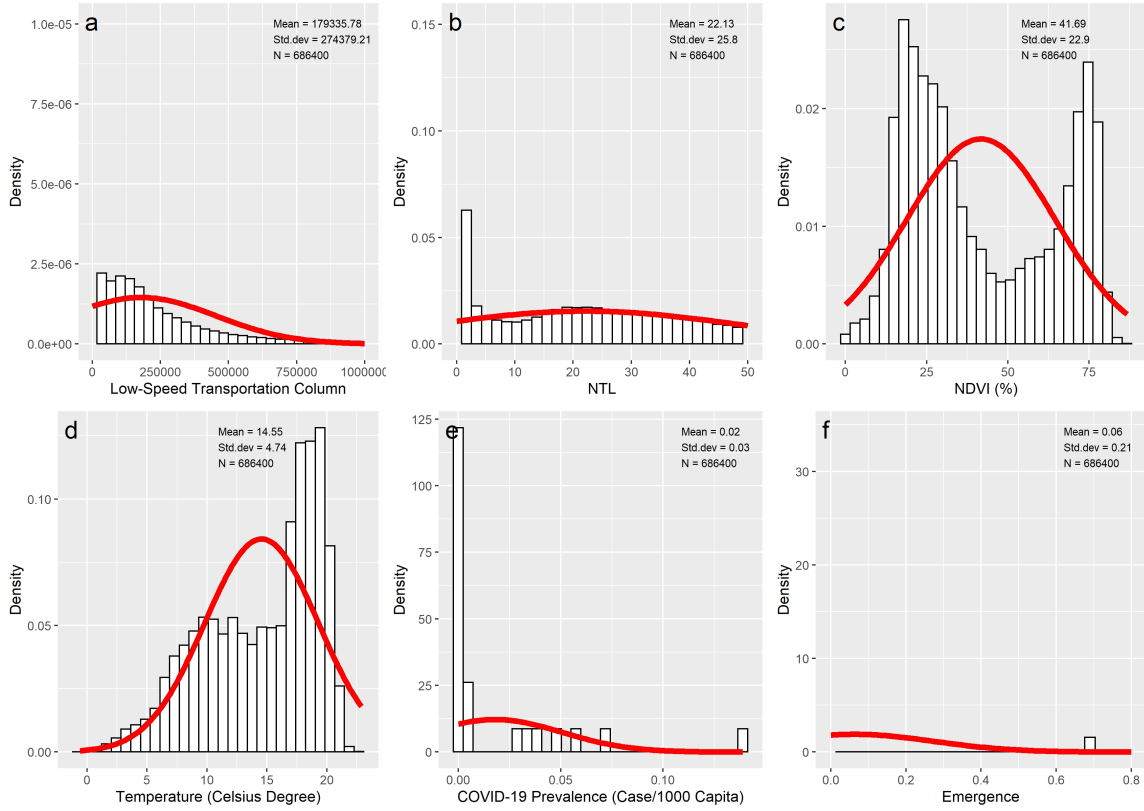


464

465 **Figure 2: Spatial Distribution of Temporally Average Low-Speed Transportation**
 466 **Column**

467 (a: the part of Tokyo on Honshu Island; b: Oshima Machi)

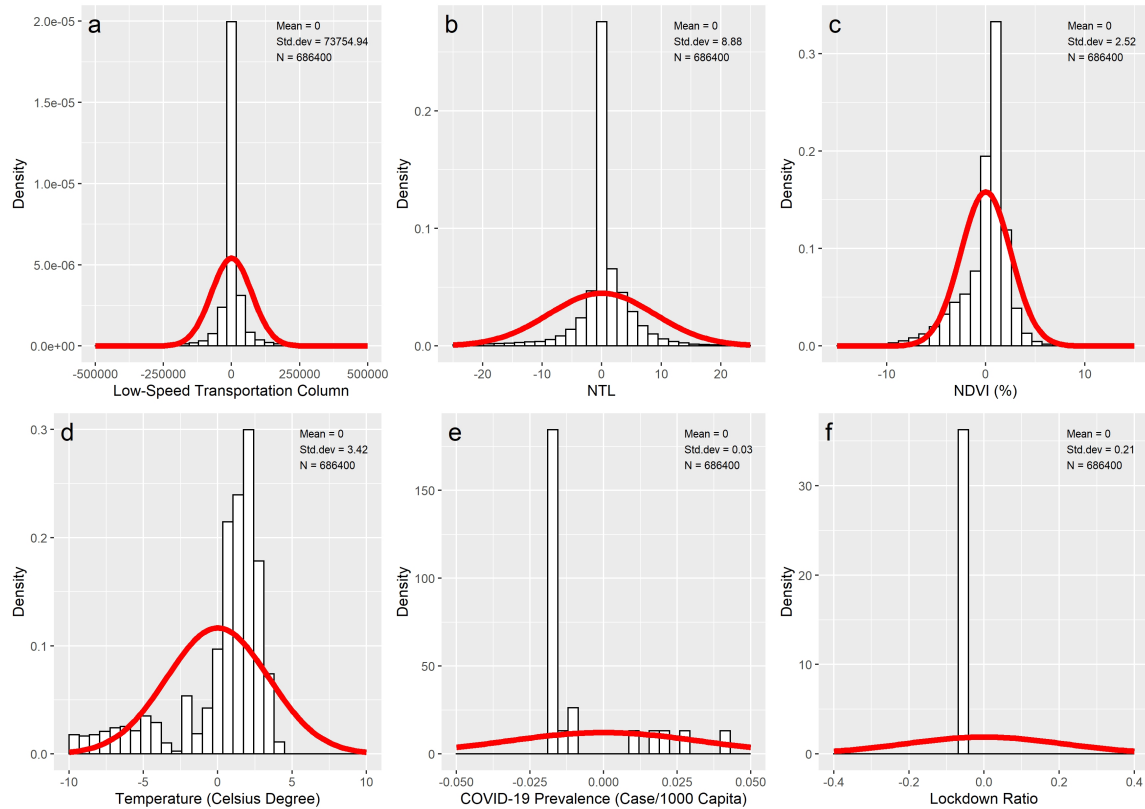
468



469

470 **Figure 3: Statistical Distributions and Descriptive Statistics of the Variables in the
471 Original Dataset**

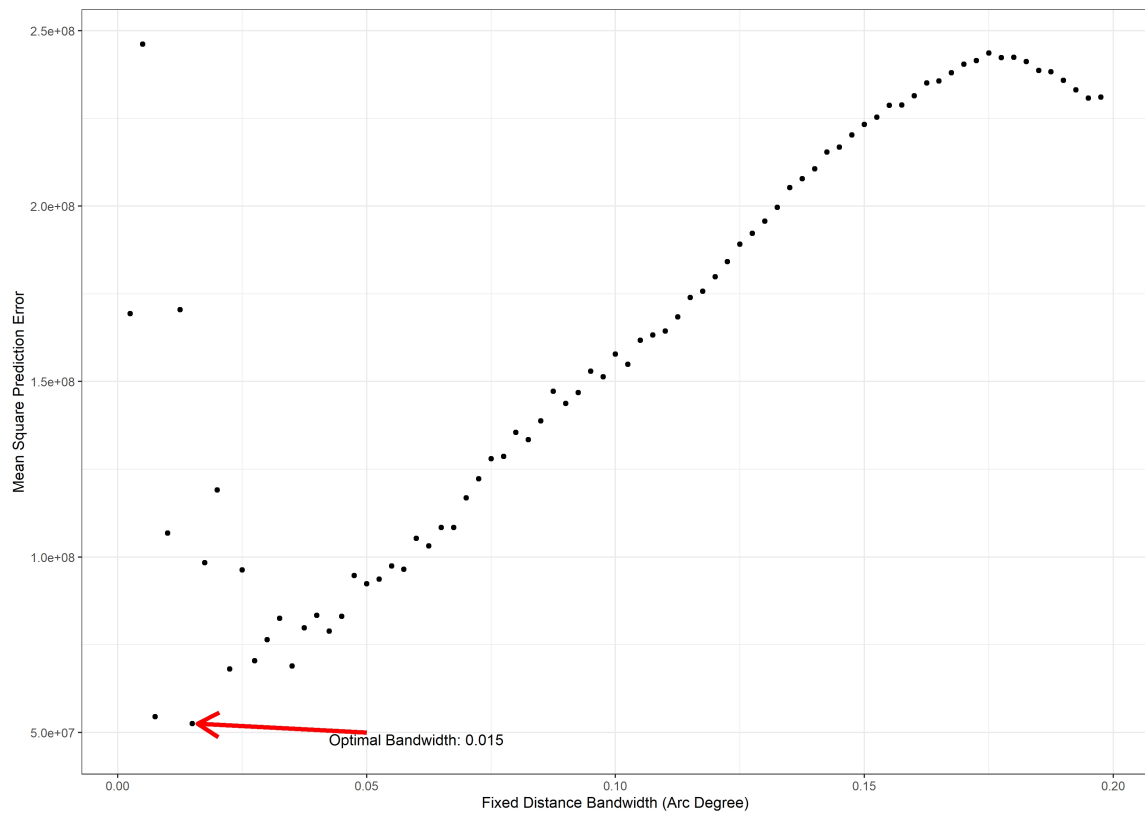
472 (The red line is the normal curve.)



473

474 **Figure 4: Statistical Distributions and Descriptive Statistics of the Variables in the
475 Transformed Dataset**

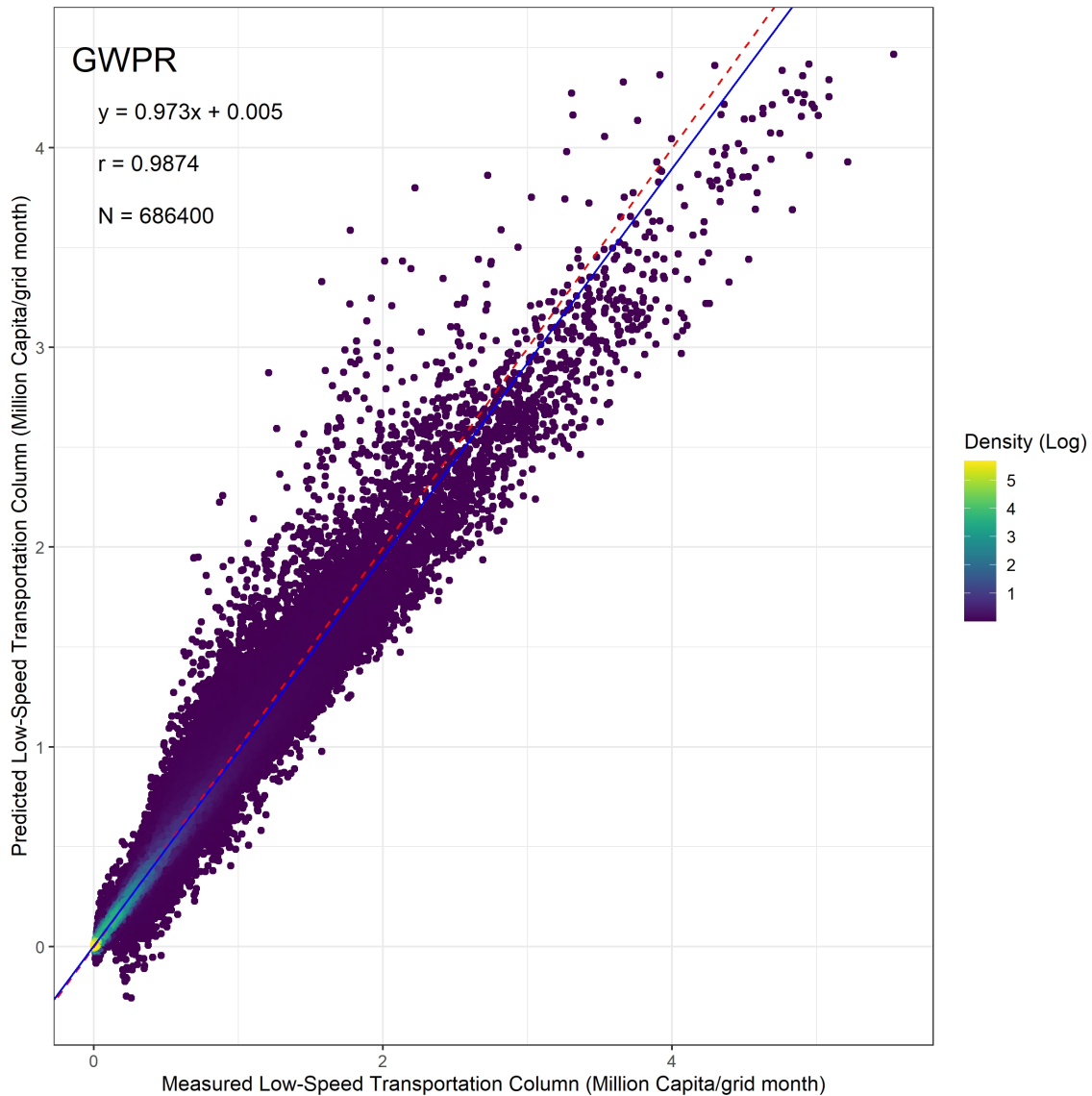
476 (The red line is the normal curve.)

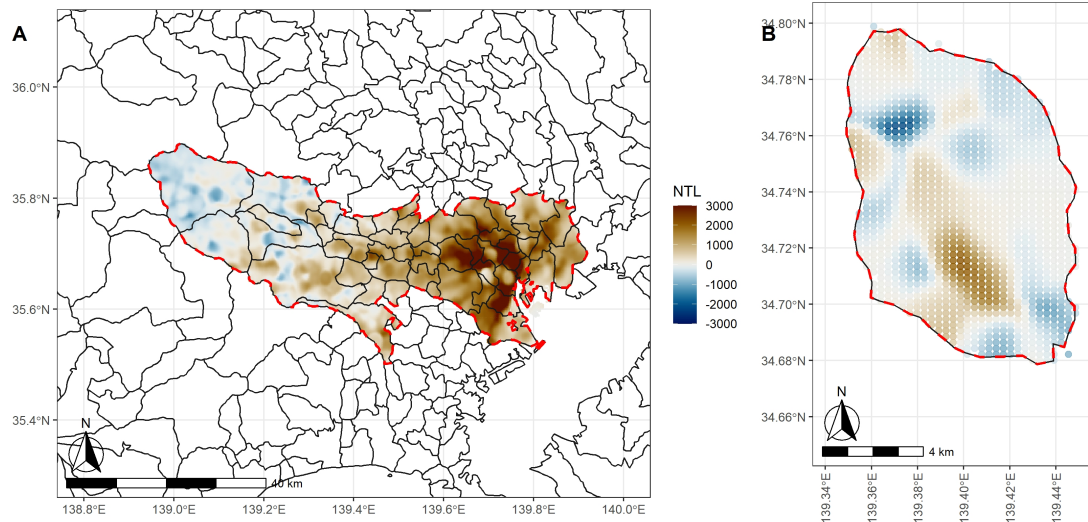


477

478

Figure 5: Step Increment Bandwidth Selection





483

484 **Figure 7: Spatial Distribution of the NTL Coefficients in GWPR**

485 (a: the part of Tokyo on Honshu Island; b: Oshima Machi)

486

487

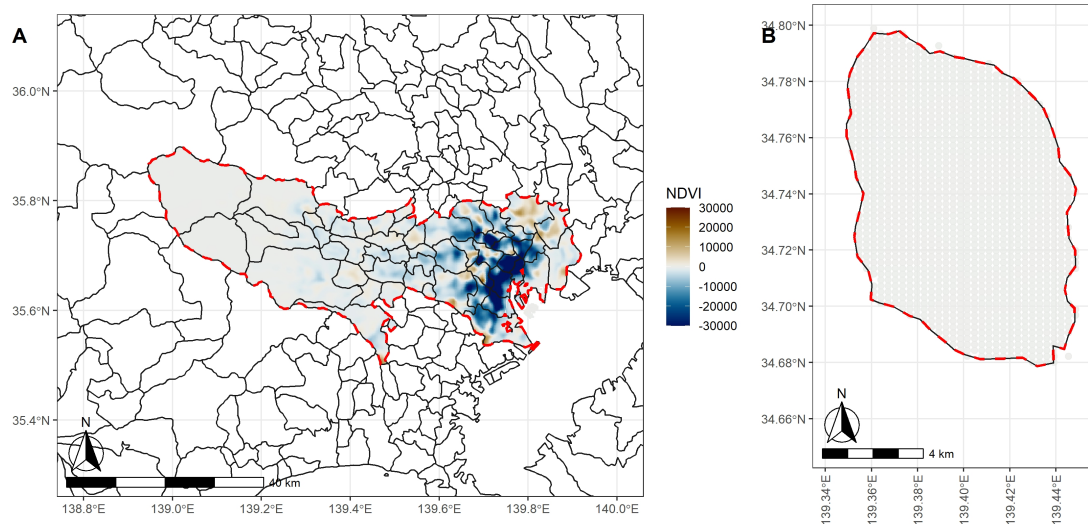
488

Figure 8: Spatial Distribution of the NDVI Coefficients in GWPR

489

(a: the part of Tokyo on Honshu Island; b: Oshima Machi)

490



491

492

493

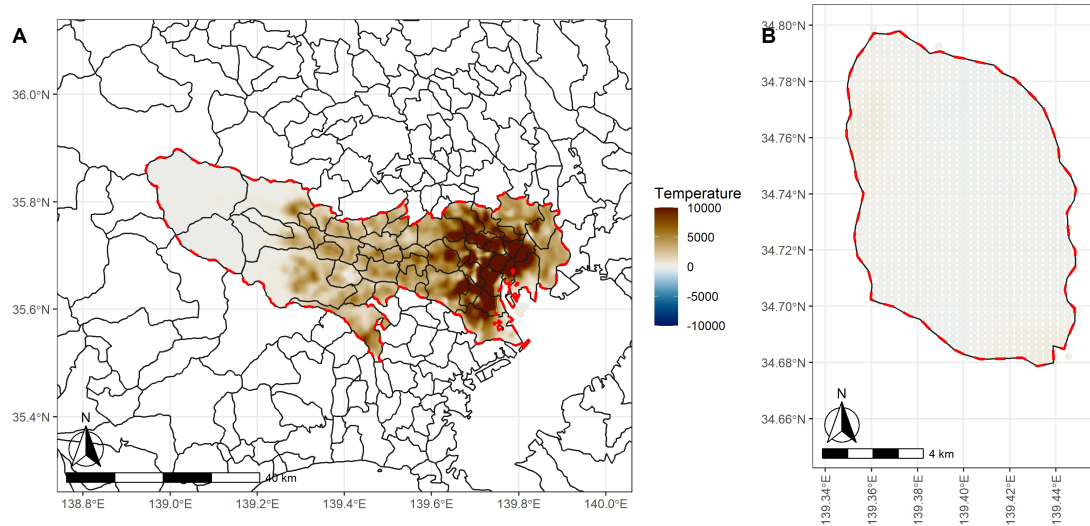
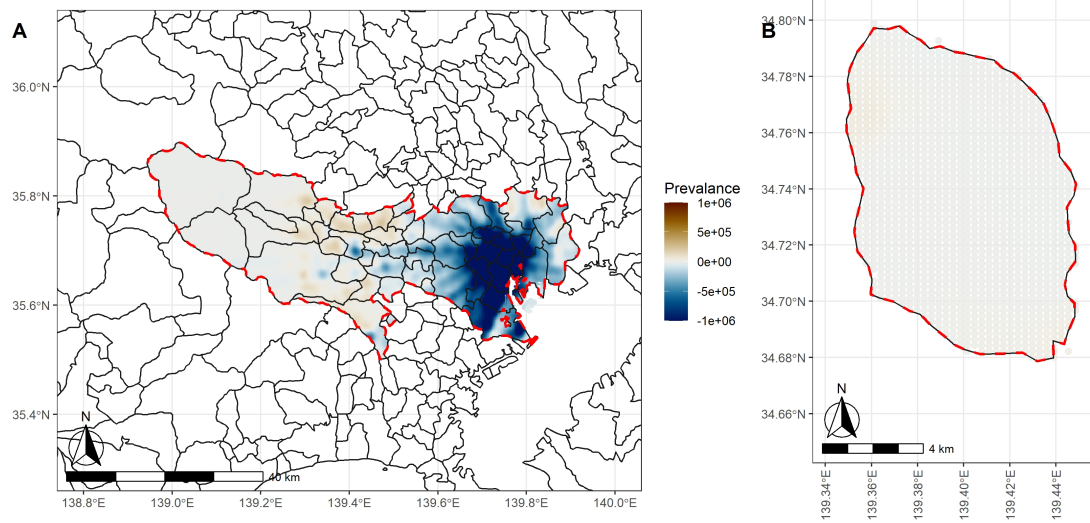


Figure 9: Spatial Distribution of the Temperature Coefficients in GWPR

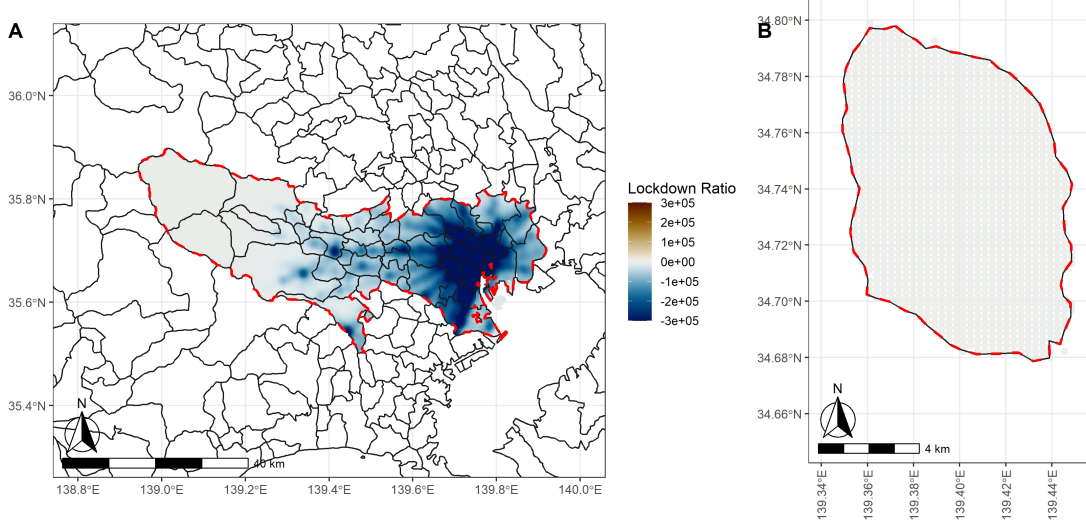
(a: the part of Tokyo on Honshu Island; b: Oshima Machi)



494

495 **Figure 10: Spatial Distribution of the COVID-19 Prevalence Coefficients in GWPR**

496 (a: the part of Tokyo on Honshu Island; b: Oshima Machi)



497

498 **Figure 11: Spatial Distribution of the COVID-19 Lockdown Ratio Coefficients in
499 GWPR**

500 (a: the part of Tokyo on Honshu Island; b: Oshima Machi)

501

502

503

504

505 **Table**

Table 1: Yearly Statistical Indicators Summary of the GWPR Results

Time	N	R ²	RMSE	MAE	r	Slope	Intercept
201901	28600	99.41%	21547.64	8771.25	0.997	0.985	2687.92
201902	28600	98.80%	29064.67	14841.01	0.997	1.056	4573.89
201903	28600	99.18%	28052.28	12135.09	0.998	0.940	1142.18
201904	28600	99.36%	24249.71	10857.27	0.998	0.952	780.33
201905	28600	99.58%	19590.87	8129.50	0.998	0.977	4563.42
201906	28600	98.86%	33247.48	10837.86	0.997	0.920	11625.83
201907	28600	97.70%	50481.55	19864.38	0.998	0.870	8539.11
201908	28600	99.61%	18713.32	8389.77	0.998	0.995	3917.57
201909	28600	99.54%	20668.98	8187.61	0.998	0.963	6676.65
201910	28600	99.02%	31890.64	11371.86	0.998	0.921	9794.22
201911	28600	98.10%	45608.14	16956.37	0.998	0.883	9236.78
201912	28600	96.03%	71089.20	30618.73	0.998	0.829	9085.48
202001	28600	98.57%	38560.32	16212.69	0.998	0.902	5192.74
202002	28600	99.45%	20878.84	8995.25	0.999	1.044	-883.64
202003	28600	97.34%	41264.44	15944.94	0.997	1.128	-8538.13
202004	28600	86.11%	48639.25	18928.48	0.937	0.983	-7428.55
202005	28600	78.14%	56266.35	17082.08	0.957	1.257	-15123.05
202006	28600	81.32%	89384.12	35791.10	0.989	1.342	-17599.45
202007	28600	98.19%	28968.43	12914.34	0.991	1.012	408.54
202008	28600	87.72%	68943.44	29769.02	0.992	1.274	-12450.61
202009	28600	94.93%	47604.19	17770.24	0.993	1.163	-9962.71
202010	28600	98.85%	26543.73	10083.90	0.997	1.064	-9145.97
202011	28600	98.65%	26614.56	11371.81	0.998	1.082	-4185.70
202012	28600	95.03%	55544.38	24676.14	0.990	0.840	5708.76
201901	686400	97.50%	43374.91	15854.20	0.987	0.973	4818.31

Note: The Ideal value of slope is 1, and the ideal value of intercept is 0.

506

507

Table 2: Statistical Indicators Summary of 10-Fold Cross Validation

	N	Statistical Indicator of Training						Statistical Indicator of Testing						
		R2	RMSE	MAE	r	Slope	Intercept	N	R2	RMSE	MAE	r	Slope	Intercept
1	61776 0	73.93 %	140216. 79	37794. 42	0.89 7	1.03 3	6000.4 06	6864 0	83.36 %	132771. 66	37033. 68	0.90 6	1.03 9	6212.2 95
2	61776 0	74.49 %	138647. 01	37584. 92	0.89 9	1.03 3	5943.2 -	6864 0	82.74 %	136029. 64	37370. 09	0.90 2	1.03 5	5985.4 35
3	61776 0	74.59 %	138389. 34	37618. 33	0.89 9	1.03 2	5783.6 11	6864 0	79.52 %	147820. 50	38866. 92	0.88 8	1.04 1	7333.3 42
4	61776 0	73.79 %	140358. 30	37867. 52	0.89 6	1.03 2	5575.5 54	6864 0	82.49 %	137841. 70	37573. 51	0.90 0	1.02 7	5600.3 49
5	61776 0	74.47 %	138671. 98	37562. 98	0.89 9	1.03 2	5776.5 53	6864 0	81.16 %	141802. 66	37774. 36	0.89 4	1.03 2	5957.5 55
6	61776 0	74.19 %	139382. 64	37586. 79	0.89 8	1.03 2	5841.4 44	6864 0	82.93 %	135531. 56	37383. 44	0.90 3	1.03 5	6198.9 43
7	61776 0	74.54 %	138325. 93	37622. 22	0.89 9	1.03 3	5883.3 43	6864 0	81.18 %	142923. 87	38049. 60	0.89 4	1.03 1	5884.5 54
8	61776 0	73.81 %	140454. 05	37787. 00	0.89 7	1.03 5	6271.1 83	6864 0	81.80 %	139447. 34	37656. 02	0.89 7	1.03 2	5674.3 39
9	61776 0	74.48 %	138353. 68	37780. 29	0.89 8	1.03 0	5310.3 70	6864 0	81.00 %	144854. 28	38361. 18	0.89 2	1.02 2	4471.2 18
10	61776 0	74.42 %	138906. 81	37690. 94	0.89 8	1.03 1	5552.2 34	6864 0	82.90 %	134582. 72	37536. 69	0.90 2	1.02 9	4808.8 79

Note: The Ideal value of slope is 1, and the ideal value of intercept is 0. When the values of statistical indicators are close between training results and testing result, the predictions of model are reliable.

510 **Reference:**

- 511 Beenstock, M., Felsenstein, D. (2019) The econometric analysis of non-stationary spatial
512 panel data. Springer.
- 513 Bellón, B., Bégué, A., Lo Seen, D., De Almeida, C., Simões, M. (2017) A Remote Sensing
514 Approach for Regional-Scale Mapping of Agricultural Land-Use Systems Based on NDVI
515 Time Series. *Remote Sensing* 9, 600.
- 516 Breusch, T.S., Pagan, A.R. (1980) The Lagrange Multiplier Test and its Applications to
517 Model Specification in Econometrics. *The Review of Economic Studies* 47, 239.
- 518 Brown, G., Schebella, M.F., Weber, D. (2014) Using participatory GIS to measure physical
519 activity and urban park benefits. *Landscape and Urban Planning* 121, 34-44.
- 520 Brunsdon, C., Fotheringham, A.S., Charlton, M.E. (2010) Geographically Weighted
521 Regression: A Method for Exploring Spatial Nonstationarity. *Geographical Analysis* 28,
522 281-298.
- 523 Brunsdon, C., Fotheringham, S., Charlton, M. (1998) Geographically Weighted Regression.
524 *Journal of the Royal Statistical Society: Series D (The Statistician)* 47, 431-443.
- 525 Calogiuri, G., Elliott, L. (2017) Why Do People Exercise in Natural Environments?
526 Norwegian Adults' Motives for Nature-, Gym-, and Sports-Based Exercise. *International
527 Journal of Environmental Research and Public Health* 14, 377.
- 528 Chen, X., Nordhaus, W.D. (2011) Using luminosity data as a proxy for economic statistics.
529 108, 8589-8594.
- 530 Chen, X., Nordhaus, W.D. (2019) VIIRS Nighttime Lights in the Estimation of Cross-
531 Sectional and Time-Series GDP. *Remote Sensing* 11, 1057.
- 532 Chen, Z., Yu, B., Ta, N., Shi, K., Yang, C., Wang, C., Zhao, X., Deng, S., Wu, J. (2019)
533 Delineating Seasonal Relationships Between Suomi NPP-VIIRS Nighttime Light and
534 Human Activity Across Shanghai, China. *IEEE Journal of Selected Topics in Applied
535 Earth Observations and Remote Sensing* 12, 4275-4283.
- 536 Chen, Z., Yu, B., Yang, C., Zhou, Y., Yao, S., Qian, X., Wang, C., Wu, B., Wu, J. (2021)
537 An extended time series (2000–2018) of global NPP-VIIRS-like nighttime light data from
538 a cross-sensor calibration. *Earth System Science Data* 13, 889-906.
- 539 Croissant, Y., Millo, G. (2008) Panel Data Econometrics in R: The plm Package. *Journal
540 of Statistical Software* 27.
- 541 Didan, K., Munoz, A.B., Solano, R., Huete, A., University of Arizona: Vegetation Index
542 Phenology Lab, (2015) MODIS vegetation index user's guide (MOD13 series).
- 543 Fotheringham, A., Brunsdon, C., Charlton, M. (2002) Geographically Weighted
544 Regression: The Analysis of Spatially Varying Relationships. John Wiley & Sons.
- 545 Fotheringham, A.S., Oshan, T.M. (2016) Geographically weighted regression and
546 multicollinearity: dispelling the myth. *Journal of Geographical Systems* 18, 303-329.
- 547 Gollini, I., Lu, B., Charlton, M., Brunsdon, C., Harris, P. (2015) GWmodel: An R package
548 for exploring spatial heterogeneity using geographically weighted models. *Journal of
549 Statistical Software* 63.
- 550 Huang, Q., Yang, X., Gao, B., Yang, Y., Zhao, Y. (2014) Application of DMSP/OLS
551 Nighttime Light Images: A Meta-Analysis and a Systematic Literature Review. *Remote
552 Sensing* 6, 6844-6866.
- 553 Jean, N., Burke, M., Xie, M., Davis, W.M., Lobell, D.B., Ermon, S. (2016) Combining
554 satellite imagery and machine learning to predict poverty. *Science* 353, 790-794.

- 555 Kang, S. (1985) A note on the equivalence of specification tests in the two-factor
556 multivariate variance components model. *Journal of Econometrics* 28, 193-203.
- 557 Krizek, K.J., Handy, S.L., Forsyth, A. (2009) Explaining Changes in Walking and
558 Bicycling Behavior: Challenges for Transportation Research. *Environment and Planning*
559 B: Planning and Design 36, 725-740.
- 560 Lan, T., Shao, G., Tang, L., Xu, Z., Zhu, W., Liu, L. (2021) Quantifying Spatiotemporal
561 Changes in Human Activities Induced by COVID-19 Pandemic Using Daily Nighttime
562 Light Data. *IEEE Journal of Selected Topics in Applied Earth Observations and Remote*
563 *Sensing* 14, 2740-2753.
- 564 Li, C., Managi, S. (2021) Spatial Variability of the Relationship between Air Pollution and
565 Well-being. *Sustainable Cities and Society*, 103447.
- 566 Li, C., Managi, S. (2022a) Estimating monthly global ground-level NO₂ concentrations
567 using geographically weighted panel regression. *Remote Sensing of Environment* 280,
568 113152.
- 569 Li, C., Managi, S. (2022b) Global malaria infection risk from climate change.
570 *Environmental Research* 214, 114028.
- 571 Li, X., Xu, H., Chen, X., Li, C. (2013a) Potential of NPP-VIIRS Nighttime Light Imagery
572 for Modeling the Regional Economy of China. *Remote Sensing* 5, 3057-3081.
- 573 Li, Z.-L., Tang, B.-H., Wu, H., Ren, H., Yan, G., Wan, Z., Trigo, I.F., Sobrino, J.A. (2013b)
574 Satellite-derived land surface temperature: Current status and perspectives. *Remote*
575 *Sensing of Environment* 131, 14-37.
- 576 Liu, Q., Sha, D., Liu, W., Houser, P., Zhang, L., Hou, R., Lan, H., Flynn, C., Lu, M., Hu,
577 T., Yang, C. (2020) Spatiotemporal Patterns of COVID-19 Impact on Human Activities
578 and Environment in Mainland China Using Nighttime Light and Air Quality Data. *Remote*
579 *Sensing* 12, 1576.
- 580 McCallum, I., Kyba, C.C.M., Bayas, J.C.L., Moltchanova, E., Cooper, M., Cuaresma, J.C.,
581 Pachauri, S., See, L., Danylo, O., Moorthy, I., Lesiv, M., Baugh, K., Elvidge, C.D., Hofer,
582 M., Fritz, S. (2022) Estimating global economic well-being with unlit settlements. *Nature*
583 *Communications* 13.
- 584 Pietrzyk-Kaszyńska, A., Czepkiewicz, M., Kronenberg, J. (2017) Eliciting non-monetary
585 values of formal and informal urban green spaces using public participation GIS.
586 *Landscape and Urban Planning* 160, 85-95.
- 587 Shi, X., Lv, F., Seng, D., Xing, B., Chen, J. (2019) Exploring the Evolutionary Patterns of
588 Urban Activity Areas Based on Origin-Destination Data. *IEEE Access* 7, 20416-20431.
- 589 Stevens, F.R., Gaughan, A.E., Linard, C., Tatem, A.J. (2015) Disaggregating Census Data
590 for Population Mapping Using Random Forests with Remotely-Sensed and Ancillary Data.
591 *Plos One* 10, e0107042.
- 592 Sun, L., Tang, L., Shao, G., Qiu, Q., Lan, T., Shao, J. (2019) A Machine Learning-Based
593 Classification System for Urban Built-Up Areas Using Multiple Classifiers and Data
594 Sources. *Remote Sensing* 12, 91.
- 595 Wang, C., Chen, Z., Yang, C., Li, Q., Wu, Q., Wu, J., Zhang, G., Yu, B. (2020) Analyzing
596 parcel-level relationships between Luojia 1-01 nighttime light intensity and artificial
597 surface features across Shanghai, China: A comparison with NPP-VIIRS data.
598 *International Journal of Applied Earth Observation and Geoinformation* 85, 101989.

- 599 Wang, X., Yan, G., Mu, X., Xie, D., Xu, J., Zhang, Z., Zhang, D. (2022) Human Activity
600 Changes During COVID - 19 Lockdown in China—A View From Nighttime Light.
601 GeoHealth 6.
- 602 Willis, A., Gjersoe, N., Havard, C., Kerridge, J., Kukla, R. (2004) Human Movement
603 Behaviour in Urban Spaces: Implications for the Design and Modelling of Effective
604 Pedestrian Environments. Environment and Planning B: Planning and Design 31, 805-828.
- 605 Wu, J., Tu, Y., Chen, Z., Yu, B. (2022) Analyzing the Spatially Heterogeneous
606 Relationships between Nighttime Light Intensity and Human Activities across Chongqing,
607 China. Remote Sensing 14, 5695.
- 608 Xiong, C., Hu, S., Yang, M., Luo, W., Zhang, L. (2020) Mobile device data reveal the
609 dynamics in a positive relationship between human mobility and COVID-19 infections.
610 Proceedings of the National Academy of Sciences 117, 27087-27089.
- 611 Yong, Z., Li, K., Xiong, J., Cheng, W., Wang, Z., Sun, H., Ye, C. (2022) Integrating
612 DMSP-OLS and NPP-VIIRS Nighttime Light Data to Evaluate Poverty in Southwestern
613 China. Remote Sensing 14, 600.
- 614 Zhong, J., Li, Z., Sun, Z., Tian, Y., Yang, F. (2020) The spatial equilibrium analysis of
615 urban green space and human activity in Chengdu, China. Journal of Cleaner Production
616 259, 120754.

617